Coordination-enhanced photochromism in dysprosium dinuclear complexes with photomodulated Single Molecule Magnet behavior

Lucie Norel, Kevin Bernot, Frédéric Gendron, Colin Gould, Thierry Roisnel, Stéphanie Delbaere, Boris Le Guennic, Denis Jacquemin, and Stéphane Rigaut

Supporting Information

Synthesis

Commercially available metallic precursors, reagents and solvents were used with no further purification and the synthesis were performed in air unless otherwise stated. ^{1}H and ^{13}C NMR spectra were recorded on a Bruker AM-400 spectrometer at 303 K at the UC Berkeley College of Chemistry Nuclear Magnetic Resonance Facility or on a Bruker Avance III HD 500 MHz at the Centre Régional de Mesures Physiques de l'Ouest. High resolution mass spectra were recorded on a Thermo Fisher Scientific Q-exactive instrument working under positive electrospray ionization mode or Bruker Maxis 4G at the Centre Régional de Mesures Physiques de l'Ouest. Elemental analysis were obtained on a Perkin Elmer 2400 Series II combustion analyser at the UC Berkeley College of Chemistry Microanalytical Facility or a Flash 1112 Thermo Fischer analyser at the Centre Régional de Mesures Physiques de l'Ouest.

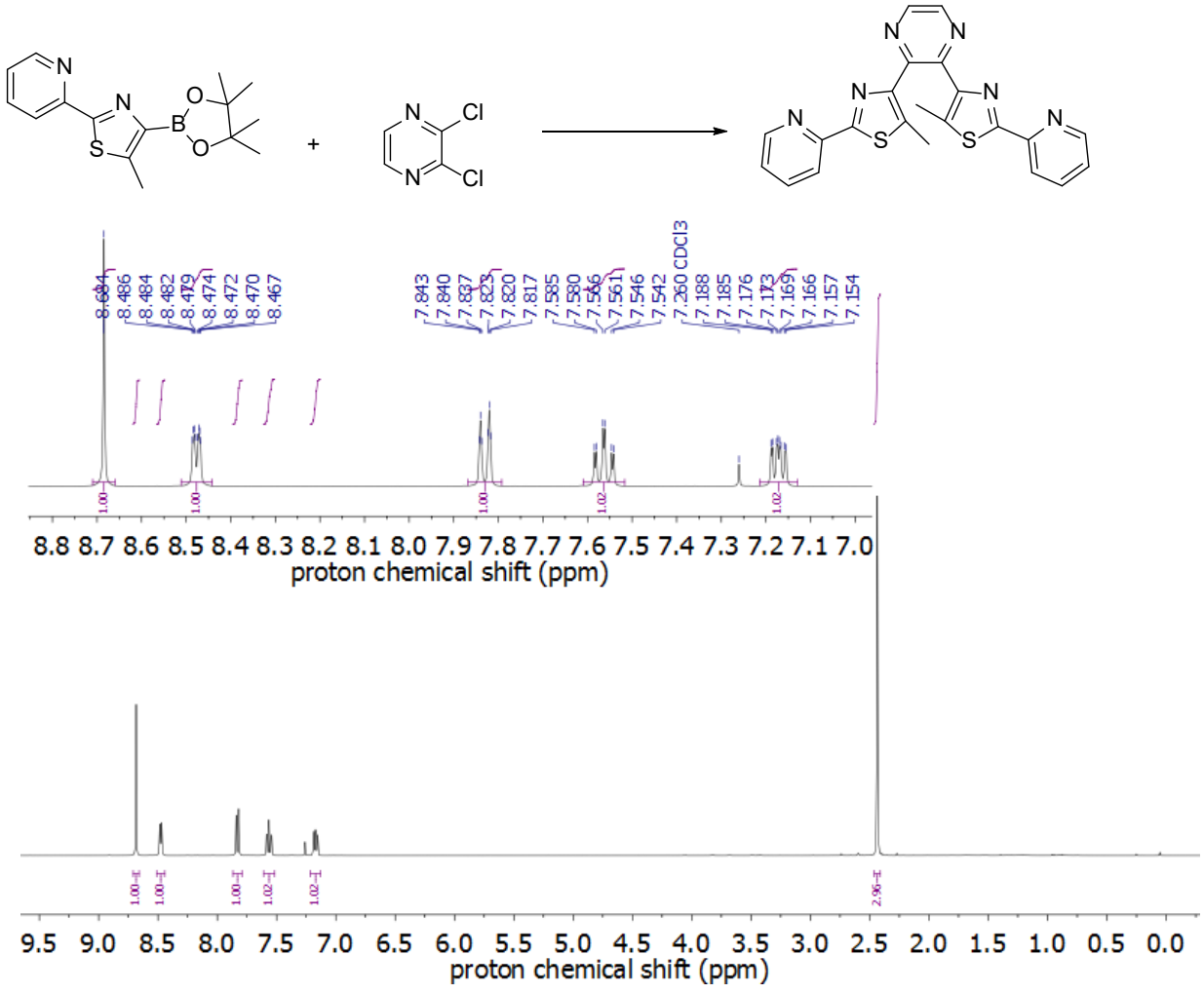

Figure S1. ^{1}H NMR spectrum of **BTP1$_o$** in $CDCl_3$.

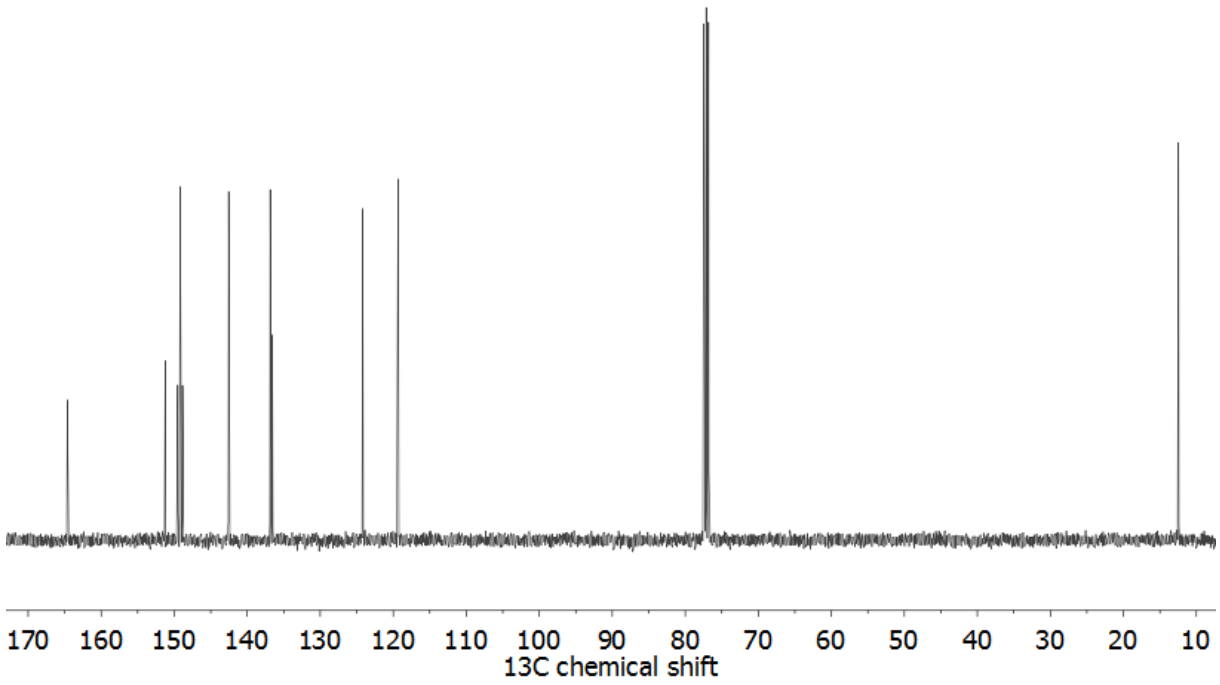

Figure S2. ^{13}C NMR spectrum of **BTP1$_o$** in $CDCl_3$.

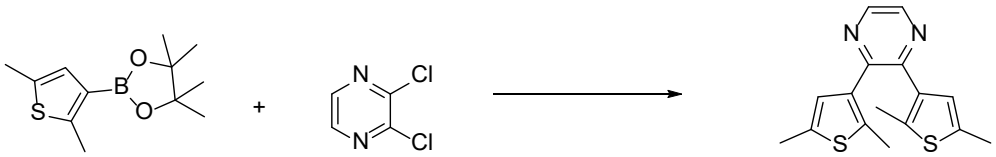

2,3-bis(2,5-dimethylthiophen-3-yl)pyrazine, BTP2$_o$. In a Schlenk tube were degassed under vacuum for 1 hour, 2,5-dimethyl-4-(4,4,5,5-tetramethyl-1,3,2-dioxaborolan-2-yl)thiophene[1] (500 mg, 2.4 mmol), 2,3-dichloropyrazine (139 mg, 0.8 mmol), $Pd_2(dba)_3$ (73 mg, 0.08 mmol), tricyclohexylphosphonium tetrafluoroborate (59 mg, 0.16 mmol), cesium fluoride (1.09 g, 7.17 mmol) and potassium carbonate (40 mg, 0.29 mmol). The solids were then dissolved in a mixture of toluene (20 mL) and water (5 mL), previously degassed by argon bubbling. The resulting reaction mixture was refluxed for 48 h and then cooled to room temperature. After the addition of water (50 mL) extraction with ethyl acetate (2×50 mL) was performed. The organic phase was filtered through a plug of celite. The celite cake was washed several times with ethyl acetate and the combined organic phases were evaporated under reduced pressure. The obtained brown oil was purified by column chromatography (silica, petroleum ether –acetone (5%)). At this stage a mixture of 2,3-bis(2,5-dimethylthiophen-3-yl)pyrazine, 2- (2,5-dimethylthiophen-3-yl)pyrazine and dba was isolated (240 mg). After a second column chromatography (silica, petroleum ether – acetone (1 -> 8%)), the product was isolated as a beige solid (66 mg, 0.22 mmol, 28 %). ^1H NMR

(400 MHz, $CDCl_3$): δ 8.53 (s, 2H), 6.52 (s, 2H), 2.38 (s, 3H), 2.15 (s, 3H). Full characterization of this compound is published elsewhere.[2]

Single Crystal XRD Studies

Details concerning the data collection and refinement can be found in the corresponding cif files and can be requested from The Cambridge Crystallographic Data Centre via www.ccdc.cam.ac.uk/data_request/cif.

Table S1. Crystal data and structure refinement parameters for **BTP1$_o$**, **1Y$_o$** and **1Dy$_o$**

	BTP1$_o$	**1Y$_o$**	**1Dy$_o$**
CCDC deposition number	1999031	1999032	1999381
Formula	$C_{22}H_{16}N_6S_2$	$C_{52}H_{22}Y_2F_{36}N_6O_{12}S_2$	$C_{52}H_{22}Dy_2F_{36}N_6O_{12}S_2$
FW	428.53	1848.69	1995.86
Cryst. Syst.	Monoclinic	Monoclinic	Monoclinic
Space group	P 2/c	C 2/c	C 2/c
a (Å)	6.5950(4)	15.0886(6)	15.1087(19)
b (Å)	9.5775(6)	22.5029(9)	22.719(3)
c (Å)	16.1965(10)	19.1937(7)	19.314(2)
α (°)	90	90	90
β (°)	97.021(3)	92.886(2)	92.666(5)
γ (°)	90	90	90
V (Å^3)	1015.36(11)	6508.7(4)	6622.4(14)
Z	2	4	4
D_{ca} (g.cm^{-3})	1.402	1.887	2.002
T (K)	100 K	100 K	150 K
Final R ($I > 2\sigma$)	0.0301	0.0282	0.0697
R_w (all)	0.0812	0.0681	0.1710

The Continuous shape measures calculation performed on **1Dy$_o$** indicates a spherical capped square antiprism (0.876) rather than a muffin (1.042), a spherical tricapped trigonal prism (1.663) or a capped square antiprism J10 (2.091) geometry.

Photoisomerization

UV-vis irradiations were performed in quartz UV cells with fluorescent tubes used for TLC illumination.

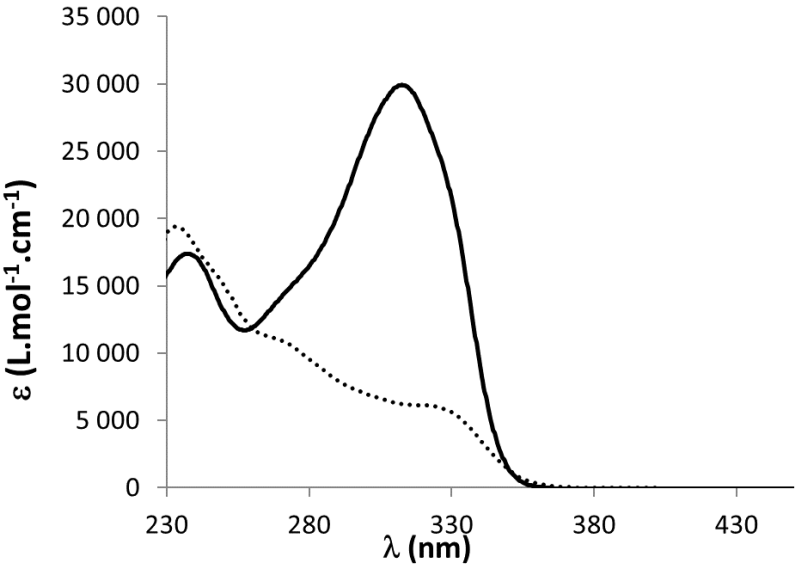

Figure S3. Electronic Absorption spectra of **BTP1$_o$** (solid line) and **BTP2** (dotted line) in acetonitrile. No modifications of the spectra were observed upon 254 nm or 365 nm irradiation.

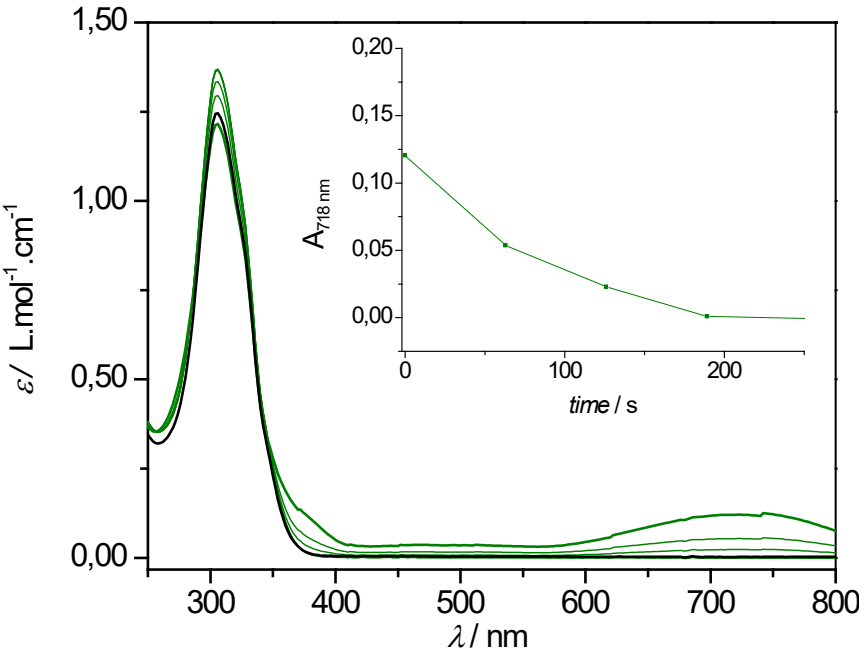

Figure S4. Electronic absorption spectra of **1Y$_o$** (black line) in dichloromethane. The green spectra correspond of the evolution of **1Y$_c$** with time after 365 nm irradiation of the solution of **1Y$_o$**. The inset show the corresponding decrease of the absorbance at 718 nm. Exponential fitting of this curve provides a half-life of 53 s at room temperature (around 26 °C).

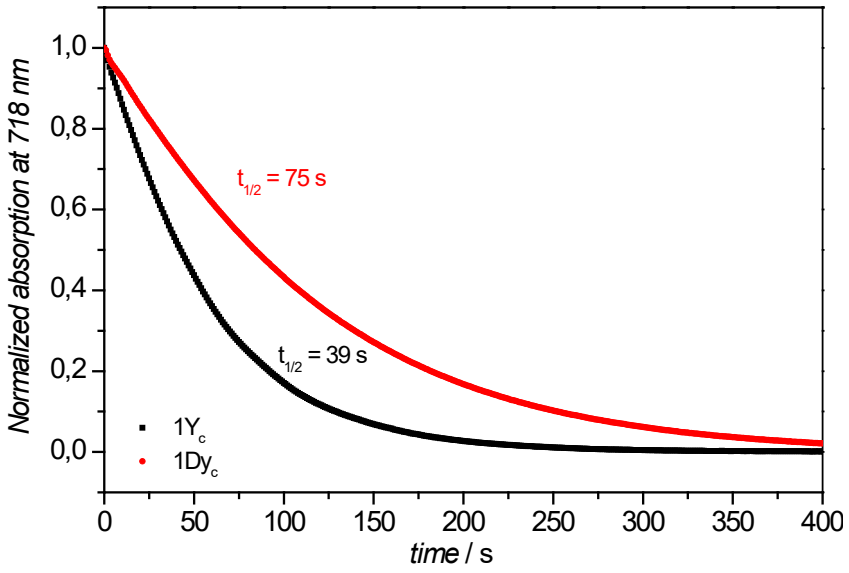

Figure S5. Evolution of the absorbance at 718 nm with time after UV irradiation generating **1Y$_c$** and **1Dy$_c$** (the temperature of the room was 28 °C). Exponential fitting of the curves provide half-life values written on each curve.

Photoisomerization studied by NMR spectroscopy

Photoirradiation was carried out directly into the NMR tube in a home-built apparatus. The emission spectrum of a 1000 Watt Xe-Hg high-pressure short-arc lamp (Newport), filtered by a band-pass glass filter (Lot Quantum Design 011FG09 : 259 < λ < 388 nm with λ_{max} = 330 nm and T = 79 %) or a heating absorbing glass filter (Lot Quantum Design KG1 : 300 < λ < 800 nm) and interferential filter (λ = 313 nm and T = 17 %, λ = 365 nm and T = 30 %) was focused on the end of a silica light-pipe (length 6 cm, diameter 8 mm), leading the light to the spinning sample tube, inserted in a quartz dewar. The temperature of the sample was controlled with a variable temperature unit (B-VT1000-Bruker, over a range of 123 to 423 K). After irradiation, the NMR sample tube was rapidly transferred to the NMR probe where experiments were acquired.

To follow the time-evolution of concentrations, the NMR irradiated sample was kept in the spectrometer at controlled temperature and ^{1}H NMR spectra were recorded at regular time intervals for a long period. In each recorded spectrum, well-resolved signals characteristic of each compound were integrated and the sum was normalized to the value of 100 % or to the initial value of concentration in mol L^{-1} (mass balance respected).

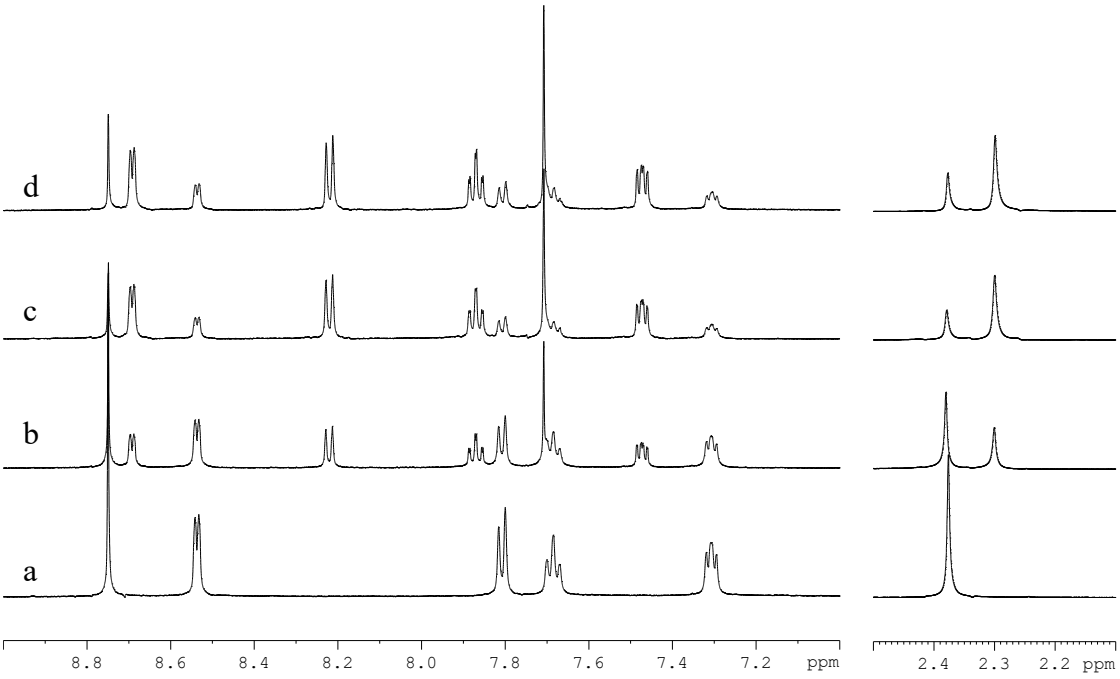

Figure S6. Evolution of the ^{1}H NMR spectrum of **BTP1o** in CD_2Cl_2 (a) upon 313 nm irradiation at 223 K for 3 min (b), 8 min (c) and then resting at 40 min at 223 K (d).

Magnetometry

Sample preparation

Since **1Dy$_c$** is not stable at room temperature, we set up a procedure to prepare it by UV irradiation at low temperature. The conditions for irradiation were optimized on the diamagnetic **1Y$_o$** analog to allow a precise estimation of the photoconversion by proton NMR and then the exact same procedure was followed with the **1Dy$_o$** complex. The low volume of the NMR sample and limited solubility of the compound in dichloromethane explain that only small amounts of compound can be prepared by this method.

Preparation of **1Y$_{c'}$**: 4.0 mg of **1Y$_o$** was placed in a thin wall precision NMR tube together with 0.7 mL of CD_2Cl_2. Under argon, it was cooled down in an acetonitrile/dry ice bath (-41°C or 269 K). At this temperature, the half-life calculated with the parameters extracted from the NMR study is over 300 h. The bath and NMR tubes were placed in an illumination chamber (Luzchem) and irradiated at 365 nm (1638 lux) for 20 min. The solution turned dark green. The tube was then placed at 77 K for transport and then transferred to the NMR spectrometer already set to a temperature of 250 K. The temperature was stabilized at 250 K and the ^{1}H NMR spectrum was measured. It showed a conversion of 91 % based on the relative integration of the thiazole methyl groups of each compound (see Figure S7).

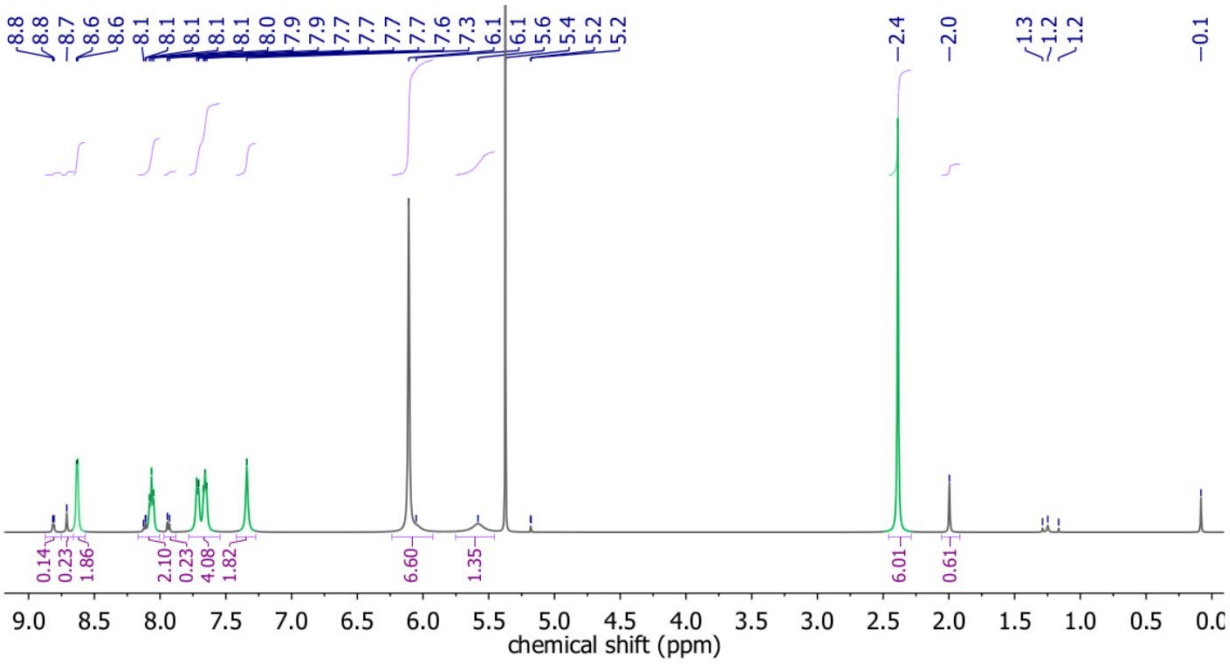

Figure S7. ^{1}H NMR spectrum of **1Y$_{c'}$** in CD_2Cl_2 prepared as described in the text, in green are shown the signals of the closed isomer.

Preparation of **1Dy$_{c'}$**: 3.9 mg of **1Dy$_o$** was placed in a thin wall precision NMR tube together with 0.8 mL of CD_2Cl_2. Under argon, it was cooled down in an acetonitrile/dry ice bath (-41°C or 269 K). The bath and NMR tubes were placed in an illumination chamber and irradiated for 20 min. The color became dark green. The solvent was then evaporated under reduced pressure, still at low temperature and the tube was then flame sealed. The tube was then placed at 77 K for transport and then transferred to the SQUID magnetometer already set to a temperature of 10 K. It is assumed that the photoconversion reached 90 % as in the case of the yttrium analog.

When the SQUID measurement was done, the tube was kept at room temperature for several days and the solid became white. It (**1Dy$_{c'}$**) was submitted to the same magnetic measurement.

Fitting procedure of the relaxation times

The temperature dependence of the relaxation time is analyzed using the general equation:

$$\tau^{-1} = \tau_{direct}^{-1} + \tau_{tunnel}^{-1} + \tau_{Raman}^{-1} + \tau_{Orbach}^{-1} \quad (1)$$

In this equation, each term relates to a different mechanism for relaxation, namely direct relaxation, quantum tunneling of magnetization, Raman relaxation and Orbach mechanism that have different temperature dependence as follow.

$$\tau^{-1} = \tau_{direct}^{-1} + \tau_{tunnel}^{-1} + BT^{n} + \tau_{0}^{-1}\exp(-U_{eff}/k_BT) \quad (2)$$

Generally, to improve the SMM behavior, the overall relaxation time should be maximized, meaning that all four contributions in equation (2) should tend to 0 and specifically for the Orbach contribution, the value of the effective energy barrier to thermal relaxation U_{eff} should be maximized. To decipher the differences in the magnetic behavior of the closed and open complexes, we have tried to analyse in detail the importance of these different contributions for each sample. First, the field dependence of τ^{-1} , that in principle should provide the τ_{direct} contribution, could not be fitted considering the usual equations and we could not extract meaningfull parameter this way (Figure S13). Similarly, and for all three samples, the Arrhenius plots shown on Figure 8 show that neither pure Orbach regime (linear behavior at high temperatures) nor tunnel regime (temperature independent behavior at low temperature) could be observed. Given the numbers of parameters in equation (2), and to avoid over-parametrization, we have first fitted **1Dy$_o$** whose high temperature behavior is the closest to a pure Orbach regime, wiith direct, quantum tunneling and Raman contributions fixed to 0. The fit above 7 K provides U_{eff} = 79.78 ± 10 K and τ_0=1.67± 1.50 10^{-9} s. These values are not fully consistent with ab-initio calculations for which ground state and first excited states are separated by ≈ 27 K or ≈ 60 K when XRD and optimized structures are considered respectively. In addition, we could not obtain a reliable fit on the whole temperature range with these Orbach parameters fixed trying to optimize the parameters for the three other regimes.

Alternatively, better fits can be found using either Orbach (free parameters), Raman and quantum tunneling contributions or Raman and quantum tunneling contributions (Figure S14). Fitting errors (R^2 and χ^2/goof values) do not provide a significant hint to choose for one or another solution (Table S2). Similar statement can be made for the other two samples, **1Dy$_{c'}$** and **1Dy$_{o'}$**. These findings illustrate why relaxation times fitting has to be made with caution when pure regimes are not clearly reached, as we already observed on photoconverted compounds.[3-4] In our particular case we propose to consider a relaxation via Raman and quantum tunneling regimes because the parameters are more consistent with values reported in the literature (**1Dy$_o$**: B= 0.110 ± 0.005 s^{-1} K^{-1}, n= 6.03 ± 0.06, τ_{tun}= 0.190 ± 0.003 s; **1Dy$_{c'}$**: B= 6.71 ± 0.60 s^{-1} K^{-1}, n= 3.49 ± 0.07, τ_{tun}= 9.3 ± 0.26 10^{-3} s; **1Dy$_{o'}$**: B= 0.61± 0.05 s^{-1} K^{-1}, n= 4.85 ± 0.08, τ_{tun}= 41 ± 0.8 10^{-3} s).[5-6]

Table S2. Table of dynamic magnetic relaxation parameters extracted for **1Dy$_o$, 1Dy$_c$**'and **1Dy$_o$'** (H_{dc} = 1200 Oe).

1Dy$_o$					
Relaxation Regime					
Orbach + Raman + Tunnel			Raman + Tunnel		
	Values	Errors		Values	Errors
τ_0 (s)	1,00 10^{-5}	3,50 10^{-6}		-	-
U_{eff} (K)	23,35	1		-	-
B ($s^{-1}.K^{-1}$)	0,28	0,16	B ($s^{-1}.K^{-1}$)	0,11	0,005
n	4,68	0,78	n	6,03	0,06
τ_{tunnel} (s)	0,22	0,03	τ_{tunnel} (s)	0,19	0,003
R^2	0,99998		R^2	0,99997	
χ^2/goof	3,29 10^{-8}		χ^2/goof	4,57 10^{-8}	
1Dy$_o$'					
Relaxation regimes					
Orbach + Raman + Tunnel			Raman + Tunnel		
	Values	Errors		Values	Errors
τ_0 (s)	1,40 10^{4}	3,00 10^{-5}	-	-	-
U_{eff} (K)	13,04	0,3	-	-	-
B ($s^{-1}.K^{-1}$)	0,03	0,03	B ($s^{-1}.K^{-1}$)	0,61	0,05
n	6,44	0,74	n	4,85	0,08
τ_{tunnel} (s)	0,034	5,00 10^{-4}	τ_{tunnel} (s)	0,041	8,00 10^{-4}
R^2	0,99998		R^2	0,99989	
χ^2/goof	3,14 10^{-9}		χ^2/goof	1,29 10^{-8}	
1Dy$_c$'					
Relaxation regimes					
Orbach + Raman + Tunnel			Raman + Tunnel		
	Values	Errors		Values	Errors
τ_0 (s)	4,84 10^{-3}	1,40 10^{-3}		-	-
U_{eff} (K)	3,41	8,64		-	-
B ($s^{-1}.K^{-1}$)	3,95	3,31	B ($s^{-1}.K^{-1}$)	6,71	0,6
N	3,8	0,45	n	3,49	0,07
τ_{tunnel} (s)	0,011	9,00 10^{-3}	τ_{tunnel} (s)	9,30 10^{-3}	2,60 10^{-4}
R^2	0,99983		R^2	0,99978	

Table S3. Relaxation times extracted for **1Dy$_o$** with H_{dc} = 1200 Oe.

T(K)	τ (μs)	T(K)	τ (μs)
1.8	109727	5	637
1.9	94225	5.5	377
2	80370	6	238
2.5	30642	6.5	155
3	10946	7	100
3.5	5003	7.5	65
4	2399	8	40
4.5	1169	8.5	18

Table S4. Adiabatic (χ_S), isothermic (χ_T) susceptibility values and relaxation times distribution (α) extracted for **1Dy$_o$** with H_{dc} = 1200 Oe.

T(K)	χ_S	χ_T	α	R^2
1.8	0.742	12.286	0.198	0.995
1.9	0.706	11.775	0.206	0.994
2	0.676	11.279	0.210	0.993
2.5	0.574	9.203	0.185	0.988
3	0.508	7.596	0.126	0.944
3.5	0.456	6.634	0.0929	0.985
4	0.424	5.889	0.0813	0.984
4.5	0.432	5.259	0.0493	0.999
5	0.409	4.764	0.0481	0.999
5.5	0.432	4.334	0.0297	0.999
6	0.400	3.989	0.0379	0.999
6.5	0.489	3.684	0.0180	0.998
7	0.459	3.433	0.0260	0.999
7.5	0.477	3.219	0.0331	0.999
8	0.632	3.015	0.0195	0.997

Table S5. Relaxation times extracted for **1Dy$_{c'}$** with H_{dc} = 1200 Oe.

T(K)	τ(μs)	R^2	T(K)	τ(μs)	R^2
1.8	6278	0.99845	6	269	0.99254
1.9	5927	0.99732	6.5	201	0.99664
2	5434	0.99696	7	182	0.99308
2.5	3644	0.99692	7.5	138	0.99323

3	2425	0.99271	8	179	0.99665
3.5	1621	0.99124	8.5	111	0.99543
4	1034	0.97770	9	124	0.99381
4.5	691	0.98950	9.5	84	0.99490
5	485	0.99169	10	171	0.99849
5.5	292	0.98431	10.5	187	0.99514

Table S6. Adiabatic (χ_S), isothermic (χ_T) susceptibility values and relaxation times distribution (α) extracted for **1Dy$_{c'}$** with H_{dc} = 1200 Oe.

T(K)	χ_S	χ_T	α	R^2
1.8	0.8822	14.6546	0.464	0.99812
1.9	0.9674	14.2268	0.453	0.99520
2	0.9449	13.7619	0.451	0.99534
2.5	1.0680	11.6996	0.423	0.99193
3	1.1103	10.0878	0.933	0.97677
3.5	1.1662	9.0360	0.402	0.99234
4	1.1172	7.9701	0.388	0.98799
4.5	1.2878	7.0999	0.360	0.99014
5	1.4058	6.4222	0.343	0.99526
5.5	1.4417	5.8275	0.326	0.98871
6	1.6783	5.3452	0.293	0.99317
6.5	1.7656	4.9525	0.287	0.99371
7	2.0051	4.6096	0.254	0.98750
7.5	2.0736	4.3249	0.259	0.97811
8	2.1841	4.0737	0.272	0.96108
8.5	2.3040	3.8278	0.250	0.97567
9	2.2979	3.6157	0.247	0.97792

Table S7. Relaxation times extracted for **1Dy$_{o'}$** with H_{dc} = 1200 Oe.

T(K)	τ(μs)	R^2	T(K)	τ(μs)	R^2
1.8	28319	0.98858	6	278	0.99683
1.9	26161	0.98692	6.5	224	0.99926
2	23992	0.98919	7	155	0.99941
2.5	12915	0.98811	7.5	108.2	0.99926
3	6576	0.98760	8	94.4	0.99951

3.5	3602	0.99143	8.5	59.02	0.99942
4	1974	0.99393			
4.5	1095	0.99570			
5	670	0.99655			
5.5	457	0.99848			

Table S8. Adiabatic (χ_S), isothermic (χ_T) susceptibility values and relaxation times distribution (α) extracted for **1Dy$_{o'}$** with H_{dc} = 1200 Oe.

T(K)	χ_S	χ_T	α	R^2
1.8	0.71638	8.06185	0.238	0.96706
1.9	0.70064	7.82713	0.232	0.95880
2	0.66946	7.61158	0.244	0.96267
2.5	0.58075	6.4750	0.2266	0.96007
3	0.51019	5.53743	0.207	0.9622
3.5	0.45084	4.92881	0.203	0.97699
4	0.4747	4.35148	0.176	0.98464
4.5	0.39615	3.88445	0.180	0.99296
5	0.47408	3.4703	0.142	0.99692
5.5	0.48486	3.15085	0.126	0.99438
6	0.40665	2.88605	0.131	0.99319
6.5	0.55657	2.66803	0.095	0.99553
7	0.41255	2.50618	0.152	0.99484
7.5	0.32858	2.35816	0.179	0.98486

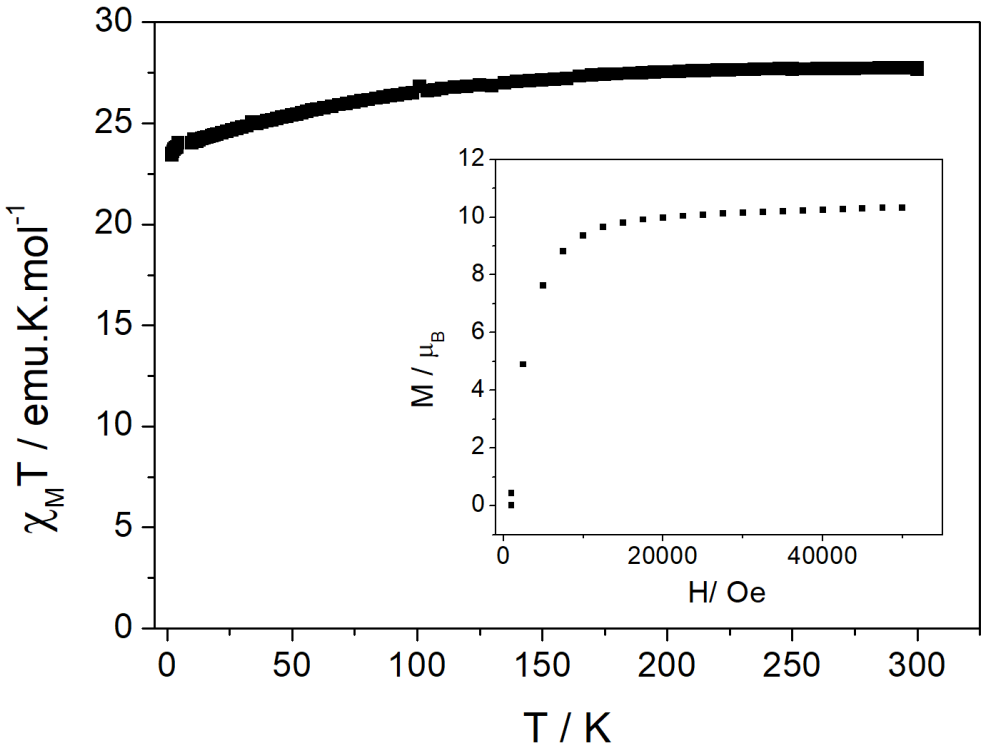

Figure S8. Temperature dependence of **1Dy$_o$** measured with a static magnetic field of 1000 Oe. In inset, field dependence of the magnetization measured at 2K.

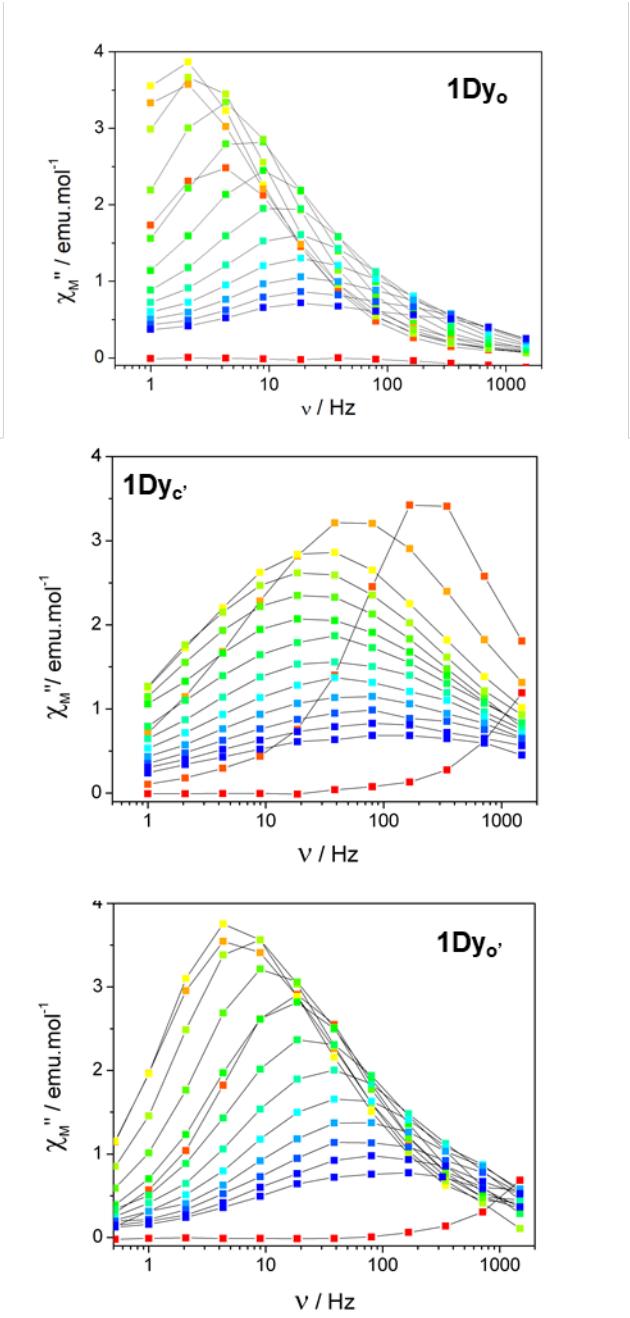

Figure S9. Field dependence of the out-of-phase magnetic susceptibility χ_M" of **1Dy$_o$, 1Dy$_{c'}$** and **1Dy$_{o'}$** (from top to bottom) measured at 2K from 0 Oe (red) to 5200 Oe (blue).

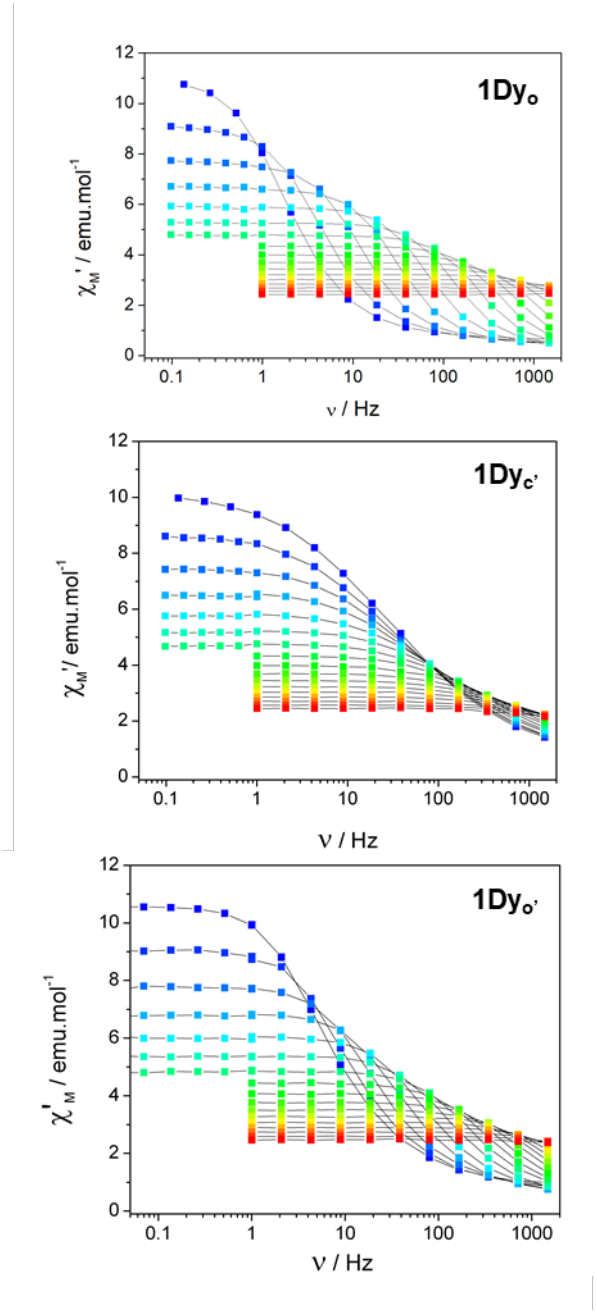

Figure S10. Frequency dependence of the in-phase magnetic susceptibility χ_M' of **1Dy$_o$, 1Dy$_{c'}$** and **1Dy$_{o'}$** (from top to bottom) measured with a static magnetic field H_{dc} = 1200 Oe for temperature from 2K (blue) to 10K (red).

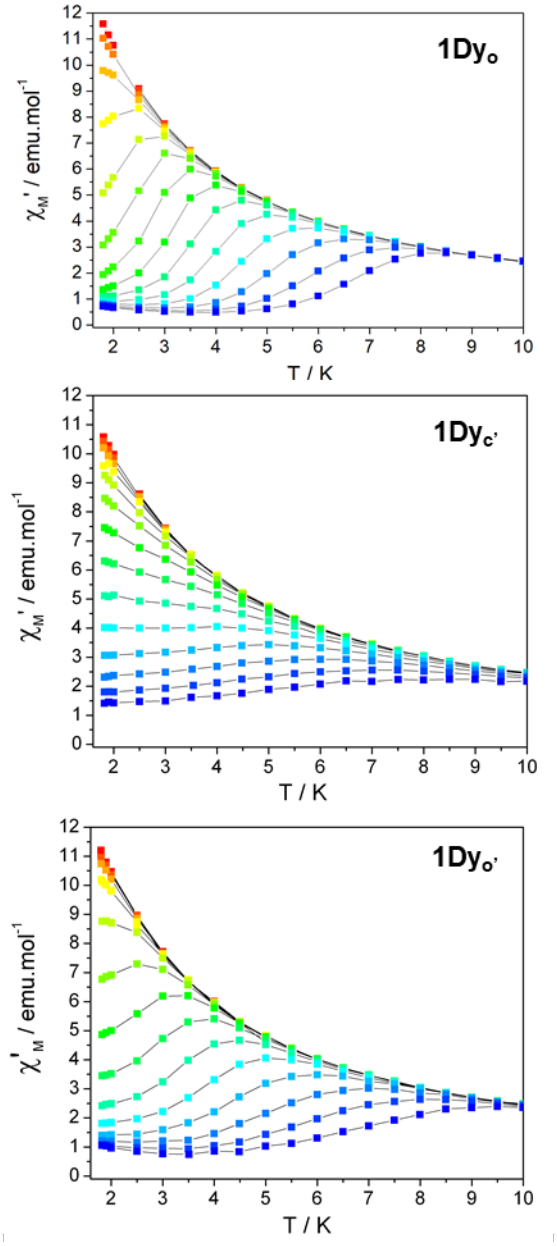

Figure S11. Temperature dependence of the in-phase magnetic susceptibility χ_M' of **1Dy$_o$, 1Dy$_{c'}$** and **1Dy$_{o'}$** (from top to bottom) measured with a static magnetic field H_{dc} = 1200 Oe and frequencies from 0.1Hz (red) to 1500Hz (blue).

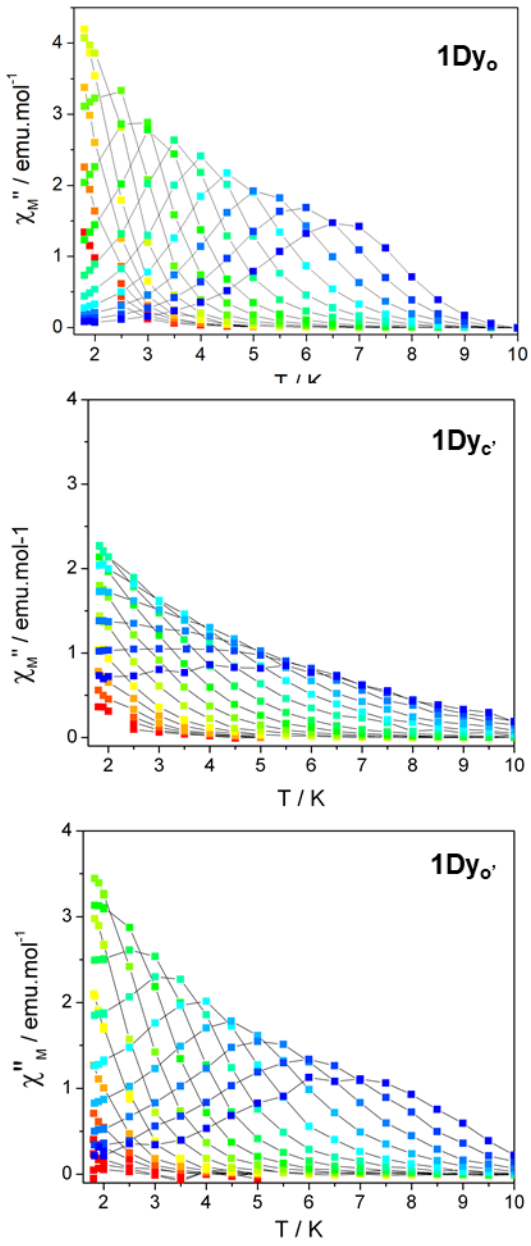

Figure S12. Temperature dependence of the out-of-phase magnetic susceptibility χ_M" of **1Dy$_o$, 1Dy$_{c'}$** and **1Dy$_{o'}$** (from top to bottom) measured with a static magnetic field H_{dc} = 1200 Oe and frequencies from 0.1Hz (red) to 1500Hz (blue).

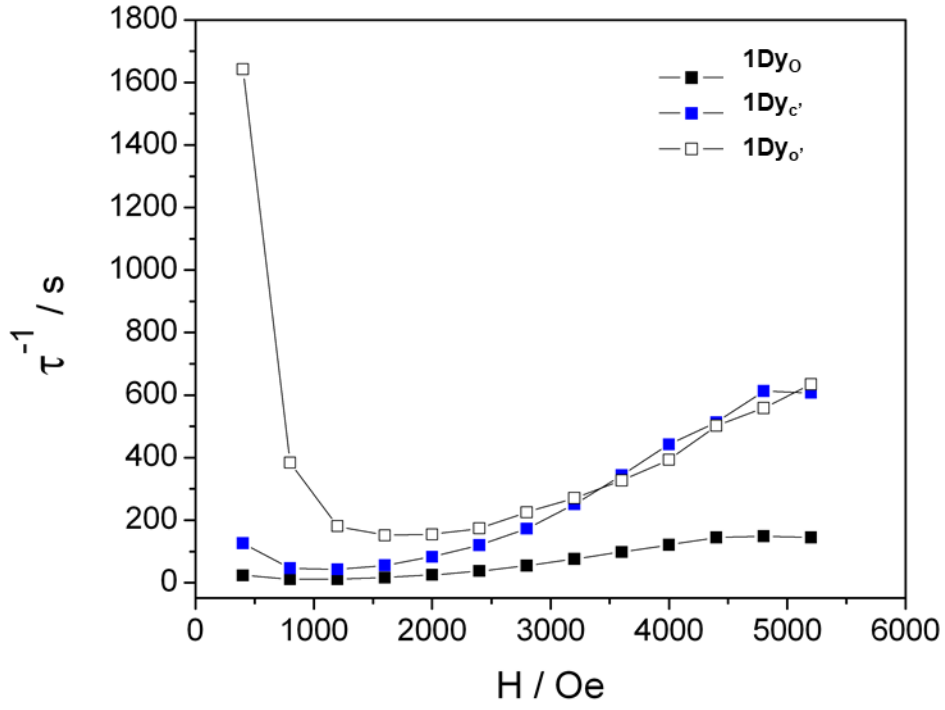

Figure S13. Field dependence of the relaxation time of **1Dy$_o$, 1Dy$_{c'}$** and **1Dy$_{o'}$** measured at 2K.

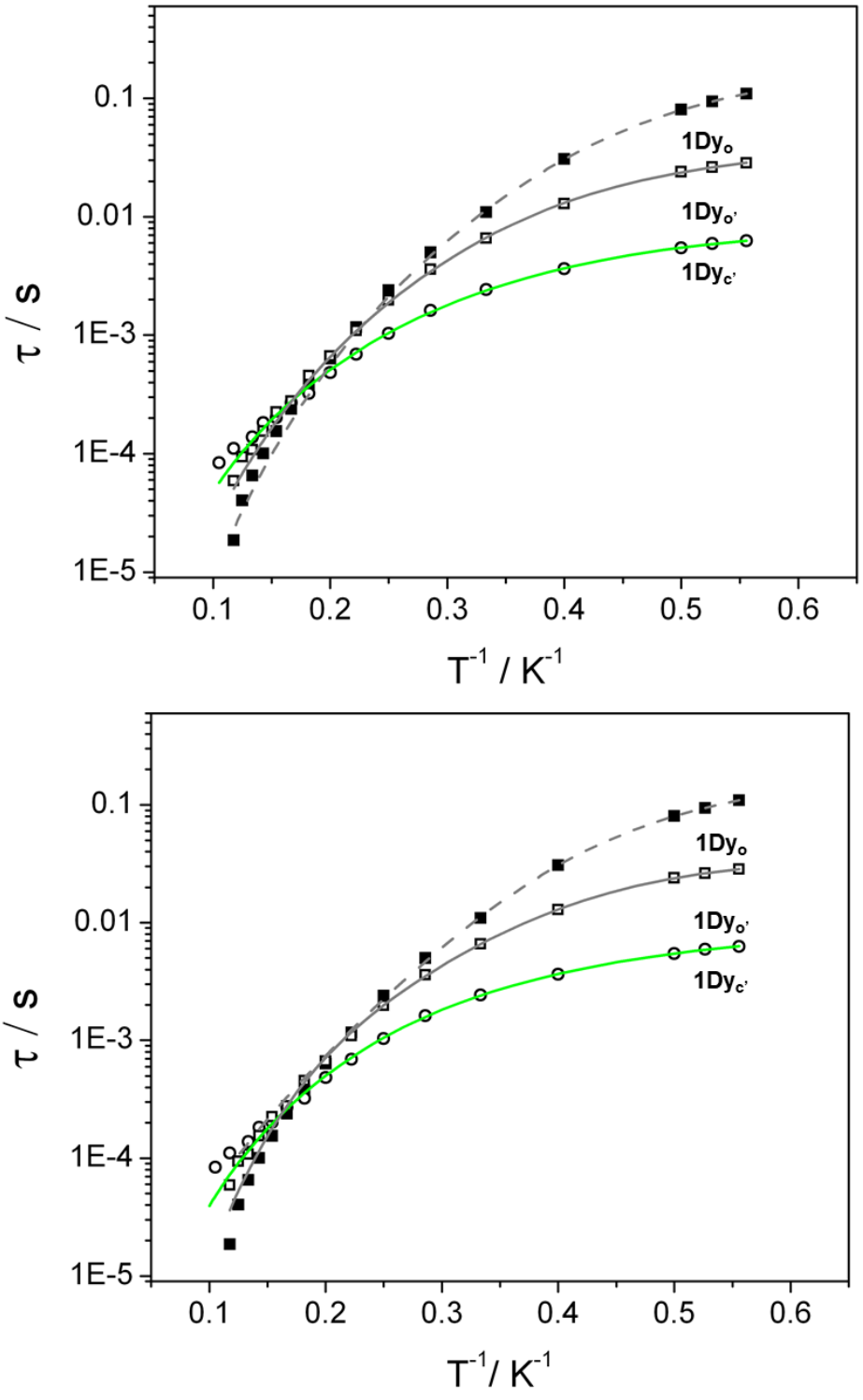

Figure S14. Arrhenius plot of the relaxation time τ and best fits using either Raman + Tunnel regimes (top, see also Figure 8) and Orbach + Raman + Tunnel (bottom). Values are detailed in Table S2.

Computational Details

Ligand

The DFT calculations on the ligand have been performed with the Gaussian 16.A03 suite of program,[7] using default procedure, algorithms and thresholds, but for what is noted below. Our calculations consisted in conformational search (full optimizations starting from several chemically-intuitive conformers) though geometry optimizations performed with the so-called tight threshold (rms forces < 1 x 10^{-5} au) followed by analytic Hessian calculations, and search for the thermal transition state, the latter being performed in the so-called broken-symmetry (BS) DFT approach to allow the suitable modelling of the single-bond breaking. We used the ωB97X[8] functional and the 6-311G(d,p) basis set for all our calculations and applied tightened SCF convergence threshold (1 x 10^{-10} au) and the *ultrafine* integration grid throughout. The solvent effects were accounted for using the well-known Polarizable Continuum Model (PCM, acetonitrile).[9] The optimal structures are displayed in Figure S15, whereas Table S9 gives the relative energies and Boltzmann weight.

Table S9. Nature, symmetry and relative free energies (w.r.t. the most stable structure) for the DFT computed conformation of ligand. On the right-hand side, we provide the Boltzmann population at RT. See Figure S15 for representation.

Conf.	Nature	Symmetry	ΔG (kcal.mol^{-1})	%age (RT)
AP1	Anti-P	C_2	11.82	0.0
AP2	Anti-P	C_2	2.47	1.4
AP3	Anti-P	C_1	6.69	0.0
P1	P	C_1	10.32	0.0
P2	P	C_1	1.25	10.6
P3	P	C_1	5.93	0.0
P4	P	C_1	5.22	0.0
P5	P	C_2	8.66	0.0
P6	P	C_2	0.00	88.0
P7	P	C_1	4.17	0.0
CL1	Closed	C_2	44.05	--
CL2	Closed	C_2	35.71	--
CL3	Closed	C_1	39.35	--

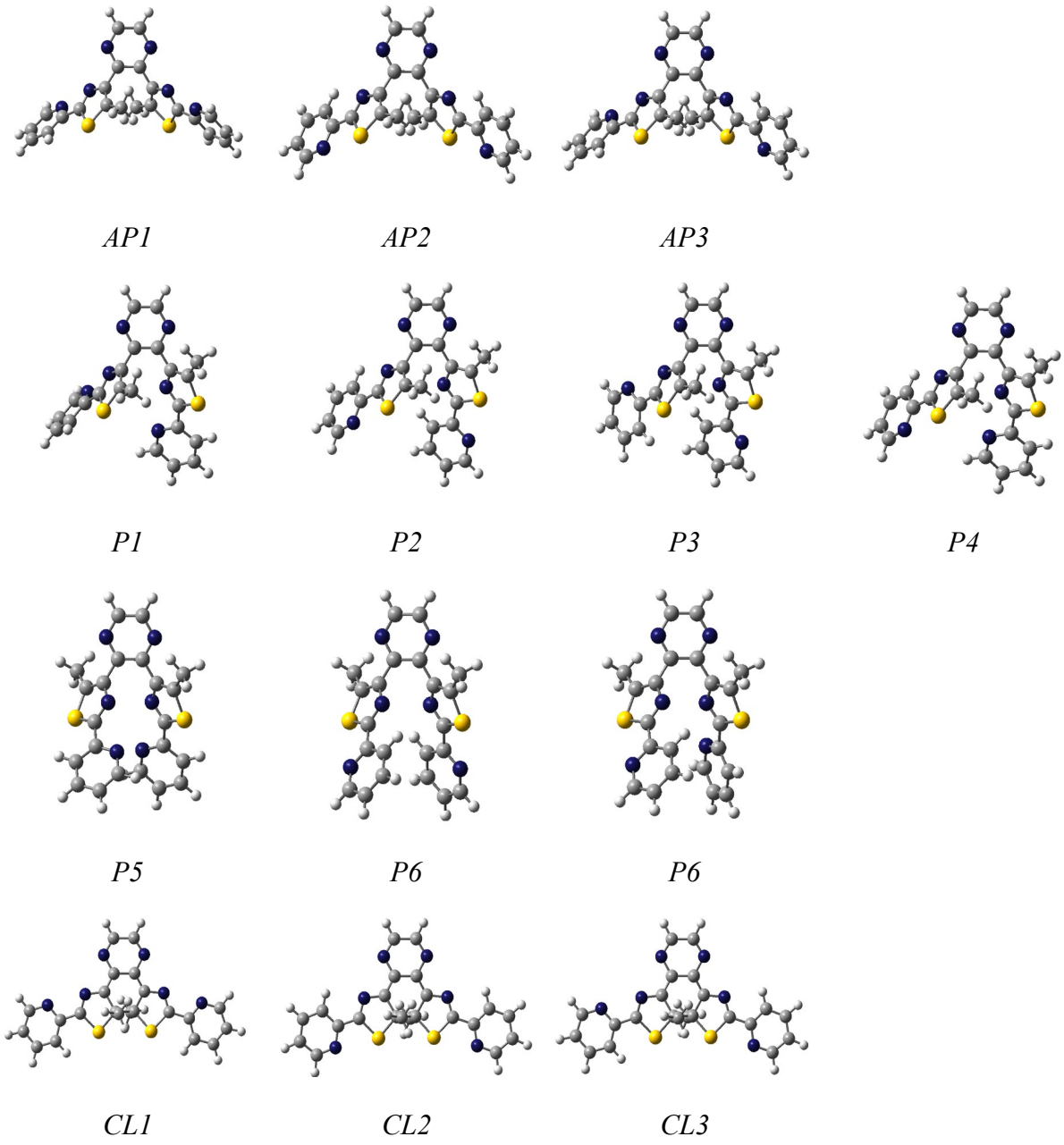

Figure S15. Representation of DFT-optimized conformers of the ligand.

Complexes

The multi-configurational calculations were performed on the crystal XRD structure of **1Dy$_o$** (labeled **1Dy$_o$-XRD**) and on optimized structures of both the open and closed forms, namely **1Dy$_o$-DFT** and **1Dy$_c$-DFT**, respectively. The structure optimizations were carried out at the Kohn-Sham density functional theory (DFT) level with the Amsterdam Density Functional (ADF[10-12]) software package. In these calculations, the Dy^{3+} centers were replaced by Y^{3+} centers, which allows to treat properly the dimers with DFT as closed-shell systems. Additionally, it is worth mentioning that in a coordination 9, the ionic radius of the Y^{3+} ion is closer to the one of Dy^{3+} than those of La^{3+} of Lu^{3+}.[13] The scalar all-electron zeroth-order regular approximation (ZORA[14]) was employed for the treatment of the scalar relativistic effects. The PBE[15-16] functional (Perdew-Burke-Ernzerhof) from the generalized gradient approximation, was used along with the triple-ζ polarized Slater-type orbital (STO) all-electron basis set with one set of polarization function for all atoms (TZP[17]). The resulting optimized structures are shown in Figure S16. It worth mentioning that the optimized open structure was calculated lower in energy by 1.040 eV (100.4 $kJ.mol^{-1}$) than the optimized closed structure.

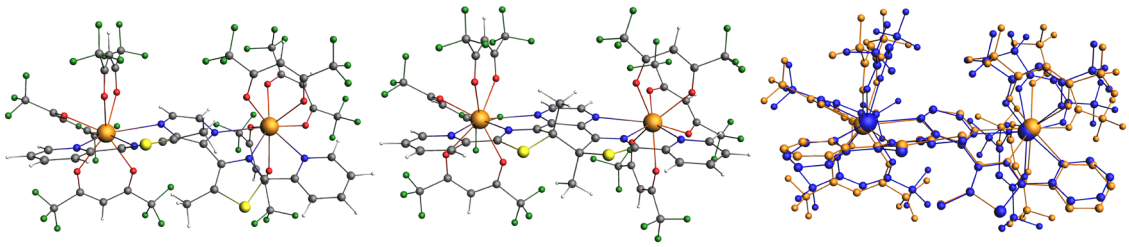

Figure S16. (left) Optimized structure of **1Dy$_o$-DFT**, (middle) optimized structure of **1Dy$_c$-DFT**, (right) overlay of the optimized structure of **1Dy$_o$-DFT** (orange) and the crystal XRD structure of **1Dy$_o$-XRD** (blue).

The Continuous shape measures calculation performed on **1Dy$_o$-DFT** indicates a muffin (0.96) rather than a spherical capped square antiprism (1.18), a spherical tricapped trigonal prism (1.75) or a capped square antiprism J10 (2.46) geometry.

The Continuous shape measures calculation performed on **1Dy$_o$-DFT** indicates a muffin (1.29) rather than a spherical capped square antiprism (1.64), a spherical tricapped trigonal prism (1.89) or a capped square antiprism J10 (2.83) geometry.

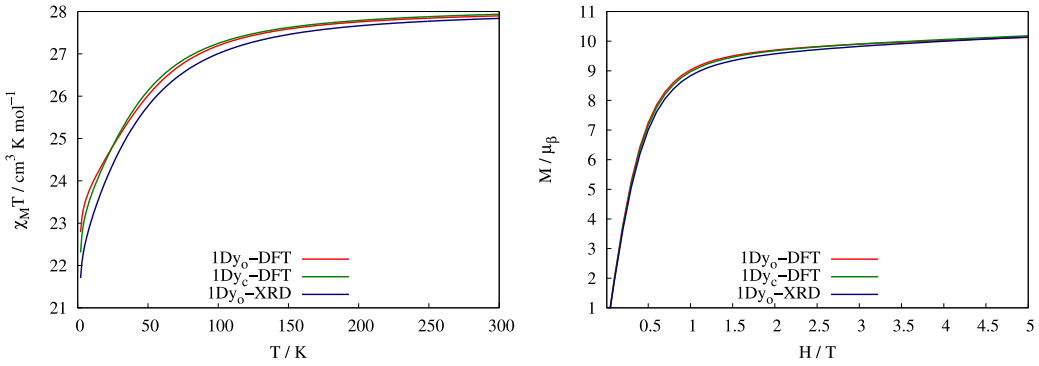

Figure S17. (left) Calculated magnetic susceptibility times temperature (χT in cm^3 K mol^{-1}) as a function of the temperature for the open and closed forms of **1Dy$_o$**. (right) Calculated magnetization (M in μB) as a function of the magnetic field.

Table S10. Calculated relative energies (ΔE in cm^{-1}) and EPR g-factors for the lowest Kramer doublet states deriving from the $^6H_{15/2}$ level of the Dy^{3+} ion in **1Dy$_o$-XRD**, **1Dy$_o$-DFT** and **1Dy$_c$-DFT**.

	1Dy$_o$-XRD [(a)]				**1Dy$_o$-DFT**[(b)]				**1Dy$_c$-DFT**[(b)]			
	ΔE	g_1	g_2	g_3	ΔE	g_1	g_2	g_3	ΔE	g_1	g_2	g_3
GS	0	0.12	0.55	18.89	0	0.02	0.05	19.40	0	0.08	0.15	19.25
ES1	39	0.05	0.39	18.67	87	1.47	4.27	14.88	66	0.78	1.47	17.58
ES2	89	0.67	1.04	17.09	108	0.85	2.92	16.22	101	0.80	2.19	15.65
ES3	137	3.60	4.63	10.92	125	1.38	7.47	8.93	128	3.01	6.09	10.11
ES4	175	0.45	4.26	13.39	169	2.40	3.99	10.25	179	2.45	2.90	10.44
ES5	211	3.46	3.91	10.79	215	1.05	1.22	16.26	233	0.36	0.44	16.01
ES6	296	1.04	1.34	16.33	267	0.40	0.46	17.06	290	0.23	0.27	17.07
ES7	434	0.06	0.08	19.49	429	0.00	0.01	19.56	469	0.00	0.00	19.65

(a) XRD structure. (b) Optimized structure.

The wavefunction theory (WFT) calculations were performed with the help of the Molcas 8.2 and OpenMolcas software packages.[18] In these calculations, the complete active space self-consistent field[19] (CASSCF) approach was used to treat the static correlation effects arising from the partially filled *4f* shell of the Dy^{3+} ion. The second-order Douglas-Kroll-Hess[20-23]scalar relativistic (SR)

Hamiltonian was used to treat the scalar relativistic effects in combination with the all-electron atomic natural orbital relativistically contracted (ANO-RCC) basis set from the Molcas library.[24-26] The basis sets were contracted to the triple-ζ plus polarization (TZP) quality for the Dy, N and O atoms (Dy = 25s22p15d11f4g2h/8s7p4d3f2g1h; N, O = 14s9p5d3f2g/4s3p2d1f), and to the double-ζ quality for the H, C and F atoms (H = 8s4p3d1f/2s ; C = 14s9p5d3f2g/3s2p, F = 14s9p5d3f2g/3s2p,). The calculations employed the state-averaged formalism at the SR level by taking into account the 21 sextet, the 224 quartet and the 490 doublet spin states arising from the 9 electrons spanning the seven 4f orbitals (i.e. CAS(9,7)). The spin-orbit coupling (SOC) was then introduced within a state interaction among the basis of calculated SR states using the restricted active space state interaction (RASSI) approach.[27] Herein the SOC matrix is diagonalized using the calculated 21 SR sextet, 224 SR quartet and the 98th lowest SR doublet spin states. The EPR *g*-factors were calculated according to reference[28] as implemented in the RASSI module of Molcas, whereas the magnetic susceptibility and magnetization calculations were performed using the Single-Aniso and Poly-Aniso modules of Molcas as detailed in reference[29].

References

(1) Gavrel, G.; Yu, P.; Léaustic, A.; Guillot, R.; Métivier, R.; Nakatani, K., 4,4′-Bithiazole-based tetraarylenes: new photochromes with unique photoreactive patterns. *Chem. Commun.* **2012,** *48* (81), 10111-10113.
(2) Milić, J. V.; Schaack, C.; Hellou, N.; Isenrich, F.; Gershoni-Poranne, R.; Neshchadin, D.; Egloff, S.; Trapp, N.; Ruhlmann, L.; Boudon, C.; Gescheidt, G.; Crassous, J.; Diederich, F., Light-Responsive Pyrazine-Based Systems: Probing Aromatic Diarylethene Photocyclization. *J. Phys. Chem. C* **2018,** *122* (33), 19100-19109.
(3) Selvanathan, P.; Dorcet, V.; Roisnel, T.; Bernot, K.; Huang, G.; Le Guennic, B.; Norel, L.; Rigaut, S., trans to cis photo-isomerization in merocyanine dysprosium and yttrium complexes. *Dalton Trans.* **2018,** *47* (12), 4139-4148.
(4) Hojorat, M.; Al Sabea, H.; Norel, L.; Bernot, K.; Roisnel, T.; Gendron, F.; Le Guennic, B.; Trzop, E.; Collet, E.; Long, J. R.; Rigaut, S., Hysteresis Photomodulation via Single-Crystal-to-Single-Crystal Isomerization of a Photochromic Chain of Dysprosium Single-Molecule Magnets. *J. Am. Chem. Soc.* **2019**.
(5) Meng, Y.-S.; Jiang, S.-D.; Wang, B.-W.; Gao, S., Understanding the Magnetic Anisotropy toward Single-Ion Magnets. *Acc. Chem. Res.* **2016,** *49* (11), 2381-2389.
(6) Liddle, S. T.; van Slageren, J., Improving f-element single molecule magnets. *Chem. Soc. Rev.* **2015,** *44* (19), 6655-6669.
(7) Frisch, M. J.; Trucks, G. W.; Schlegel, H. B.; Scuseria, G. E.; Robb, M. A.; Cheeseman, J. R.; Scalmani, G.; Barone, V.; Petersson, G. A.; Nakatsuji, H.; Li, X.; Caricato, M.; Marenich, A. V.; Bloino, J.; Janesko, B. G.; Gomperts, R.; Mennucci, B.; Hratchian, H. P.; Ortiz, J. V.; Izmaylov, A. F.; Sonnenberg, J. L.; Williams; Ding, F.; Lipparini, F.; Egidi, F.; Goings, J.; Peng, B.; Petrone, A.; Henderson, T.; Ranasinghe, D.; Zakrzewski, V. G.; Gao, J.; Rega, N.; Zheng, G.; Liang, W.; Hada, M.; Ehara, M.; Toyota, K.; Fukuda, R.; Hasegawa, J.; Ishida, M.; Nakajima, T.; Honda, Y.; Kitao, O.; Nakai, H.; Vreven, T.; Throssell, K.; Montgomery Jr., J. A.; Peralta, J. E.; Ogliaro, F.; Bearpark, M. J.; Heyd, J. J.; Brothers, E. N.; Kudin, K. N.; Staroverov, V. N.; Keith, T. A.; Kobayashi, R.; Normand, J.; Raghavachari, K.; Rendell, A. P.; Burant, J. C.;

Iyengar, S. S.; Tomasi, J.; Cossi, M.; Millam, J. M.; Klene, M.; Adamo, C.; Cammi, R.; Ochterski, J. W.; Martin, R. L.; Morokuma, K.; Farkas, O.; Foresman, J. B.; Fox, D. J. *Gaussian 16 Rev. A.03*, Wallingford, CT, 2016.
(8) Chai, J.-D.; Head-Gordon, M., Systematic optimization of long-range corrected hybrid density functionals. *J. Chem. Phys.* **2008,** *128* (8), 084106.
(9) Tomasi, J.; Mennucci, B.; Cammi, R., Quantum Mechanical Continuum Solvation Models. *Chem. Rev.* **2005,** *105* (8), 2999-3094.
(10) te Velde, G.; Bickelhaupt, F. M.; Baerends, E. J.; Fonseca Guerra, C.; van Gisbergen, S. J. A.; Snijders, J. G.; Ziegler, T., Chemistry with ADF. *J. Comput. Chem.* **2001,** *22* (9), 931-967.
(11) Fonseca Guerra, C. F.; Snijders, J. G.; te Velde, G.; Baerends, E. J., Towards an order-N DFT method. *Theor. Chem. Acc.* **1998,** *99* (6), 391-403.
(12) Baerends, E. J.; Ziegler, T.; Atkins, A. J.; Autschbach, J.; Bashford, D.; Baseggio, O.; Bérces, A.; Bickelhaupt, F. M.; Bo, C.; Boerritger, P. M.; Cavallo, L.; Daul, C.; Chong, D. P.; Chulhai, D. V.; Deng, L.; Dickson, R. M.; Dieterich, J. M.; Ellis, D. E.; van Faassen, M.; Ghysels, A.; Giammona, A.; van Gisbergen, S. J. A.; Goez, A.; Götz, A. W.; Gusarov, S.; Harris, F. E.; van den Hoek, P.; Hu, Z. J., C. R.; Jacobsen, H.; Jensen, L.; Joubert, L.; Kaminski, J. W.; van Kessel, G.; König, C.; Kootstra, F.; Kovalenko, A.; Krykunov, M.; van Lenthe, E.; McCormack, D. A.; Michalak, A.; Mitoraj, M.; Mor- ton, S. M.; Neugebauer, J.; Nicu, V. P.; Noodleman, L.; Osinga, V. P.; Patchkovskii, S.; Pavanello, M.; Peeples, C. A.; Philipsen, P. H. T.; Post, D.; Pye, C. C.; Ramanantoan- ina, H.; Ramos, P.; Ravenek, W.; Rodríguez, J. I.; Ros, P.; Rüger, R.; Schipper, P. R. T.; Schlüns, D.; van Schoot, H.; Schreckenbach, G.; Seldenthuis, J. S.; Seth, M.; Snijders, J. G.; Solà, M.; M., S.; Swart, M.; Swerhone, D.; te Velde, G.; Tognetti, V.; Vernooijs, P.; Versluis, L.; Visscher, L.; Visser, O.; Wang, F.; Wesolowski, T. A.; van Wezenbeek, E. M.; Wiesenekker, G.; Wolff, S. K.; Woo, T. K.; Yakovlev, A. L., "ADF2017, SCM, Theoretical Chemistry, Vrije Universiteit, Amsterdam, The Netherlands, https://www.scm.com". **2017**.
(13) Shannon, R. D., Revised effective ionic radii and systematic studies of interatomic distances in halides and chalcogenides. *Acta Cryst. A* **1976,** *32* (5), 751-767.
(14) Lenthe, E. v.; Baerends, E. J.; Snijders, J. G., Relativistic regular two-component Hamiltonians. *J. Chem. Phys.* **1993,** *99* (6), 4597-4610.
(15) Perdew, J. P.; Burke, K.; Ernzerhof, M., Generalized Gradient Approximation Made Simple. *Phys. Rev. Lett.* **1996,** *77* (18), 3865-3868.
(16) Perdew, J. P.; Burke, K.; Ernzerhof, M., Generalized Gradient Approximation Made Simple [Phys. Rev. Lett. 77, 3865 (1996)]. *Phys. Rev. Lett.* **1997,** *78* (7), 1396-1396.
(17) Van Lenthe, E.; Baerends, E. J., Optimized Slater-type basis sets for the elements 1–118. *J. Comput. Chem.* **2003,** *24* (9), 1142-1156.
(18) Aquilante, F.; Autschbach, J.; Carlson, R. K.; Chibotaru, L. F.; Delcey, M. G.; De Vico, L.; Fdez. Galván, I.; Ferré, N.; Frutos, L. M.; Gagliardi, L.; Garavelli, M.; Giussani, A.; Hoyer, C. E.; Li Manni, G.; Lischka, H.; Ma, D.; Malmqvist, P. Å.; Müller, T.; Nenov, A.; Olivucci, M.; Pedersen, T. B.; Peng, D.; Plasser, F.; Pritchard, B.; Reiher, M.; Rivalta, I.; Schapiro, I.; Segarra-Martí, J.; Stenrup, M.; Truhlar, D. G.; Ungur, L.; Valentini, A.; Vancoillie, S.; Veryazov, V.; Vysotskiy, V. P.; Weingart, O.; Zapata, F.; Lindh, R., Molcas 8: New capabilities for multiconfigurational quantum chemical calculations across the periodic table. *J. Comput. Chem.* **2016,** *37* (5), 506-541.
(19) Roos, B. O.; Taylor, P. R.; Siegbahn, P. E. M., *Chem. Phys.* **1980,** *48*, 157-288.

(20) Douglas, M.; Kroll, N. M., Quantum electrodynamical corrections to the fine structure of helium. *Annals of Physics* **1974,** *82* (1), 89-155.
(21) Hess, B. A., Applicability of the no-pair equation with free-particle projection operators to atomic and molecular structure calculations. *Physical Review A* **1985,** *32* (2), 756-763.
(22) Hess, B. A., Relativistic electronic-structure calculations employing a two-component no-pair formalism with external-field projection operators. *Physical Review A* **1986,** *33* (6), 3742-3748.
(23) Wolf, A.; Reiher, M.; Hess, B. A., The generalized Douglas–Kroll transformation. *J. Chem. Phys.* **2002,** *117* (20), 9215-9226.
(24) Widmark, P.-O.; Malmqvist, P.-Å.; Roos, B. O., Density matrix averaged atomic natural orbital (ANO) basis sets for correlated molecular wave functions. *Theoretica chimica acta* **1990,** *77* (5), 291-306.
(25) Roos, B. O.; Lindh, R.; Malmqvist, P.-Å.; Veryazov, V.; Widmark, P.-O., Main Group Atoms and Dimers Studied with a New Relativistic ANO Basis Set. *J. Phys. Chem. A* **2004,** *108* (15), 2851-2858.
(26) Roos, B. O.; Lindh, R.; Malmqvist, P.-Å.; Veryazov, V.; Widmark, P.-O., New Relativistic ANO Basis Sets for Transition Metal Atoms. *J. Phys. Chem. A* **2005,** *109* (29), 6575-6579.
(27) Malmqvist, P.-å.; Roos, B. O.; Schimmelpfennig, B., *Chem. Phys. Lett.* **2002,** *357*, 230-240.
(28) Bolvin, H., An Alternative Approach to the g-Matrix: Theory and Applications. *ChemPhysChem* **2006,** *7* (7), 1575-1589.
(29) Chibotaru, L. F.; Ungur, L., Ab initio calculation of anisotropic magnetic properties of complexes. I. Unique definition of pseudospin Hamiltonians and their derivation. *J. Chem. Phys.* **2012,** *137* (6), 064112.